Journal of Wind Engineering & Industrial Aerodynamics 206 (2020) 104353

Contents lists available at ScienceDirect

Journal of Wind Engineering & Industrial Aerodynamics

journal homepage: www.elsevier.com/locate/jweia

Experimental characterisation of the wake behind paired vertical-axis wind turbines

Antoine Vergaerde [a], Tim De Troyer [a,*], Sara Muggiasca [b], Ilmas Bayati [b,c], Marco Belloli [b], Joanna Kluczewska-Bordier [d], Nicolas Parneix [d], Frederic Silvert [d], Mark C. Runacres [a]

[a] Vrije Universiteit Brussel, Pleinlaan 2, 1050, Brussels, Belgium
[b] Politecnico di Milano, Dipartimento di Meccanica, Via La Masa 1, 20156, Milano, Italy
[c] Maritime Research Institute Netherlands, Haagsteeg, 6700 AA Wageningen, the Netherlands
[d] Nenuphar, 1, Rue du Professeur Calmette, 59000, Lille, France

ARTICLE INFO

Keywords:
wake
Vertical-axis wind turbine
Wind tunnel
Experimental
Wind turbine applications
Paired wind turbines

ABSTRACT

Two vertical-axis wind turbines (VAWTs) benefit from a power increase when placed side by side in close proximity. To study the potential of paired VAWTs for integration in wind farms, wind tunnel wake measurements of lift-driven VAWTs are compared for isolated and three counter-rotating configurations. Because the wake of an isolated VAWT is deflected, the direction of rotation significantly influences the wake of paired VAWTs. The wake of counter-rotating VAWTs where the adjacent blades move downwind, exhibits a similar length, width and replenishment as the wake of an isolated VAWT. The wake of counter-rotating VAWTs with adjacent upwind moving blades, however, significantly differs from an isolated VAWT wake. While its wake length is similar to an isolated VAWT wake, its width and replenishment are not. Because of appealing wake characteristics, paired VAWTs exhibit unique advantages for wind farm applications, and especially for offshore floating wind farms.

1. Introduction

To outperform classic wind farms consisting of horizontal-axis wind turbine (HAWTs), researchers seek for optimal wind farm configurations by, e.g. slightly misaligning the HAWT rotors to induce a wake deflection (Campagnolo et al., 2016; Gebraad et al., 2016; Fleming et al., 2017). Other approaches aim to outperform current wind farms through colocation of HAWTs with vertical-axis wind turbines (VAWTs) (Kadum et al., 2020; Xie et al., 2017). To date, most existing wind farms are onshore but current trends exhibit increasing offshore exploitation (Bilgili et al., 2011) together with floating applications (Taboada, 2016; Borg and Collu, 2035; Borg et al., 2014). The platforms for such floating applications greatly impact the cost of offshore energy and, while being less efficient than HAWTs, VAWTs could be economically more viable (Tjiu et al., 2015; Paulsen et al., 2013; Hand and Cashman, 2020; Bull et al., 2014). Furthermore, placing counter-rotating VAWTs side by side in close proximity allows them to benefit from an increased power making such configurations promising for wind farm applications (Dabiri, 2011; Duraisamy and Lakshminarayan, 2014; Kinzel et al., 2012; Zanforlin and Nishino, 2016; Vergaerde et al., 2020). This benefit has inspired innovative concepts such as the placement of two counter-rotating VAWTs on a same floating platform (Parneix et al., 2016). Besides the power increase, such a setup would benefit from a zero-net generator torque and a means to orient the platform by varying the individual torques (Kanner, 2015; Kanner et al., Yeung). However, to consider paired VAWTs for wind farm applications, the characteristics of their wakes are to be assessed.

The complex aerodynamics of lift-driven VAWTs induces a wake which is influenced by i.a. unsteady separation, dynamic stall, blade-wake interaction and flow curvature effects (Rezaeiha et al., 2018a, 2018b). The wake of an isolated VAWT has extensively been studied by Simão Ferreira (Simão Ferreira, 2009) both numerically and experimentally. To date, it remains one of the most important contributions to the understanding of VAWT wakes. The experimental study of Tescione et al. (2014), through the use of particle image velocity, captured the propagation of shed vorticity in the wake and in doing so it captured the flow mechanism leading to the typical asymmetric induction field of a VAWT wake. Boudreau and Dumas (2017) compare the wake topology of a (single-bladed) HAWT and VAWT up to twelve diameters downwind. For VAWTs, they find that tip vortices propagate vertically towards mid

* Corresponding author.
E-mail address: tim.de.troyer@vub.be (T. De Troyer).

https://doi.org/10.1016/j.jweia.2020.104353
Received 20 April 2020; Received in revised form 28 July 2020; Accepted 7 August 2020
Available online xxxx

span height. This results in a spanwise contraction of the wake, which induces a horizontal expansion of the wake. Bachant and Wosnik (2015) also point out the important contribution of tip vortices for the replenishment of the wakes. They compare the tip vortices at the top of the wake to an asymmetrical doublet propelling high-velocity flow downward into the wake. Similarly, Rolin and Porté-Agel (2018) identify a pair of counter-rotating vortices in the wake of VAWTs and state that they are the most important replenishment mechanism. The study of VAWT wakes was also complemented with a CFD-investigation on the influence of pitch and surge motions induced by floating platforms (Lei et al., 2019). In that study, wave motions were found to induce a wake diversity depending on the period and amplitude of the motions.

Contributions to the understanding of experimental studies on VAWT wakes have been presented on the similarities of the wake in free stream and boundary layer flow (Abkar and Dabiri, 2017), on the influence on the wake of the driving method of the rotor (Araya and Dabiri, 2015), on the Reynolds number effect (Bachant and Wosnik, 2016), on the effect of confinement (Dossena et al., 2015) and on the possibility of scaling experimental wake measurements (Kadum et al., 2018). The experimental study by Hohman et al. (2018), on the effect of inflow conditions, allowed to conclude that the overall wake structures can be captured in uniform flow and are representative for wakes in the atmospheric boundary layer.

The wake of paired VAWTs in co- and counter-rotating configurations has also been studied before. The open-field study of Kinzel et al. (2012) investigated the velocity field along the centre line of an array of paired VAWTs. They observe that the flow velocity is recovered to 95% of its unperturbed velocity at a downwind distance of 6 diameters (compared to 4 diameters downstream of an isolated VAWT (Dabiri, 2011)). Similarly, for a HAWT wind farm, they state that minimal spacings of 14 diameters are necessary for a similar recovery. Numerical studies on the wake of paired VAWTs have also been reported, e.g. the study of Posa (2019). He compares the wake of co-rotating and counter-rotating VAWTs to the wake of an isolated VAWT. He concludes that counter-rotating configurations should be preferred because the deflection of the wake of co-rotating configurations is influenced by the value of the tip-speed ratio. In the experimental study of Lam and Peng (2016), the wake of paired VAWTs was studied but interaction between the wakes remained limited because of a relatively large inter-turbine distance. More recently, Brownstein et al. (2019) have graphically represented identified isosurfaces of the time-averaged streamwise vorticity depending on the direction of rotation of the paired VAWTs. This dependence on the direction of rotation results in very different wake characteristics.

The present study experimentally compares the wake of lift-driven isolated and paired VAWTs. Three-dimensional velocity measurements are presented over a range that, to the authors knowledge, remains unique to date. Based on these measurements, different replenishment mechanisms are identified. The study is complemented with a quantitative analysis to support and expand the understanding of the wake of paired VAWTs. A comparison with another experimental study points out the sensitivity of the wake to different operating parameters.

2. Experimental setup and measurement procedure

2.1. VAWT setup and wind tunnel setup

Two H-type Darrieus rotors with inclined struts are mounted in isolated or paired configurations for the wind tunnel tests. The rotors have a vertical span, H, of 0.8m, a diameter, D, of 0.5m and a blade chord c of 0.05m (Fig. 1). The tip-speed ratio λ is around 3 and the chord-based Reynolds number is 110000. The rotors have straight NACA0018 blades and thicker NACA0024 struts. Because of the symmetry of the rotors, it is possible to turn the rotors upside-down to reverse the direction of rotation. A floating floor was installed below the rotors to simulate a ground or water surface, see Fig. 2 (also indicated with the main dimensions). An extensive description of the experimental setup along with a thorough characterisation can be found in (Vergaerde et al., 2019).

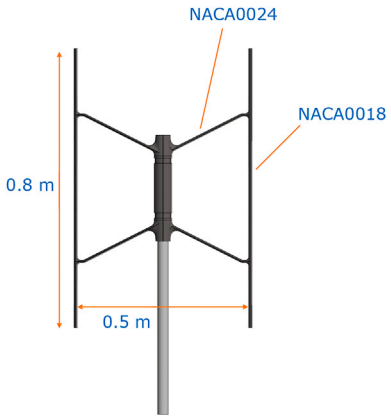

Fig. 1. Main geometric features of the VAWT rotor.

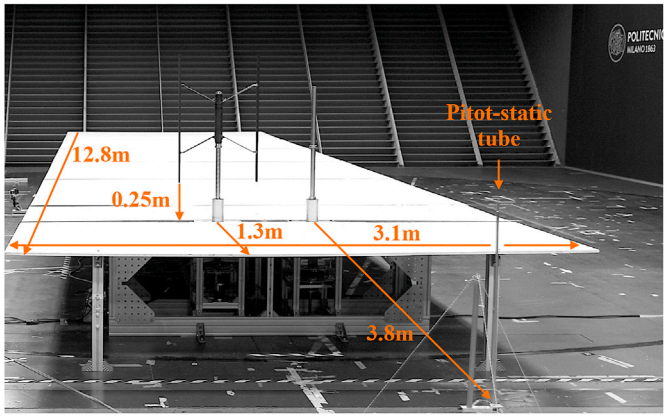

Fig. 2. Experimental setup inside the wind tunnel.

The isolated configuration is compared to three counter-rotating paired configurations. For the 1.2D and 1.3D inner-downwind configurations (1.2D I-D and 1.3D I-D), the adjacent blades move along with the wind. The distance between the rotor shafts is 1.2 and 1.3 diameters respectively. For the 1.3D inner-upwind configuration (1.3D I–U) the adjacent blades move against the wind.

2.2. Wind tunnel and measuring equipment

This study is carried out in the wind tunnel of the Politecnico di Milano (GVPM). The test section is 13.84m wide, 3.84m high and 35m long. The benefit of the large test section is twofold: a large downwind clearance behind the test setup (11.5m) and a low blockage ratio ($\approx$ 2%). Because of the small blockage ratio, no blockage corrections need to be applied (blockage corrections are negligible for values below 5% (Battisti et al., Paradiso; Howell et al., 2010; Ross and Altman, 2011)). The unperturbed incoming flow velocity U_0 is kept at 10.7 m/s with a turbulence intensity of 2% for all further described experiments.

An upwind Pitot-static tube measures the velocity of the incoming flow with an uncertainty of 0.13%, see Fig. 2. It is positioned 3.8m upstream of the turbines. A one-dimensional traverse system is used to measure the velocity in the wake behind the turbines. This traverse system moves a vertically mounted arm equipped with five sensors: four Cobra probes and one Aeroprobe Corporation-Standard omniprobe (Fig. 3). The Cobra probes and omniprobe provide three-dimensional velocity measurements of the flow field with an uncertainty of 5% and 2% respectively. The sampling frequency is 2000Hz for the Cobra probes and 500Hz for the omniprobe. A spectral analysis of the measurements indicated that the Cobra probes reliably capture frequencies up to 250Hz while the omniprobe can measure up to around 40Hz (the rotors turn at 20Hz).

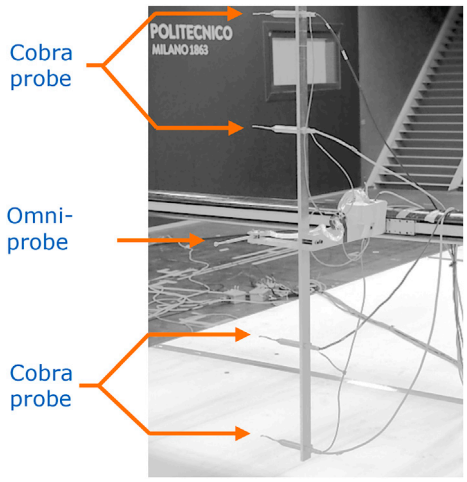

Fig. 3. A mechanical arm equipped with five sensors, is used to measure the wake behind the rotors.

2.3. Geometric convention

The linear and rotational coordinate systems are represented schematically in Fig. 4. The streamwise direction corresponds to the x-axis with the positive direction along with the incoming flow. The horizontal, lateral direction corresponds to the y-axis and goes from left to right when facing downwind. The positive z-axis points vertically upwards and $z = 0m$ corresponds to the rotor mid span. The velocity components in the x-, y- and z-direction correspond to u, v and w respectively.

The azimuthal angle θ is considered zero when the rotor is perpendicular to the wind direction (independent of the rotational direction). For $90^\circ < \theta < 270^\circ$, a blade moves along with the main wind direction, referred to as downwind moving blades. A blade moving between $270^\circ < \theta < 90^\circ$ moves against the wind direction, referred to as an upwind moving blade.

2.4. Characterised wake range

Three-dimensional velocity measurements are carried out at several downstream vertical planes, i.e. planes defined by the yz-axes (Fig. 5). For the isolated and 1.2D inner-downwind configurations, measurements were carried out at the 1D, 4D, 6D, 8D, 12D, 16D and 21D planes (expressed in rotor diameters). For the 1.3D inner-downwind and inner-upwind configurations, only the 4D, 6D and 12D planes are characterised. Two types of plane resolutions are used for the measurement (Fig. 5b) and are indicated with the corresponding lines on Fig. 5a.

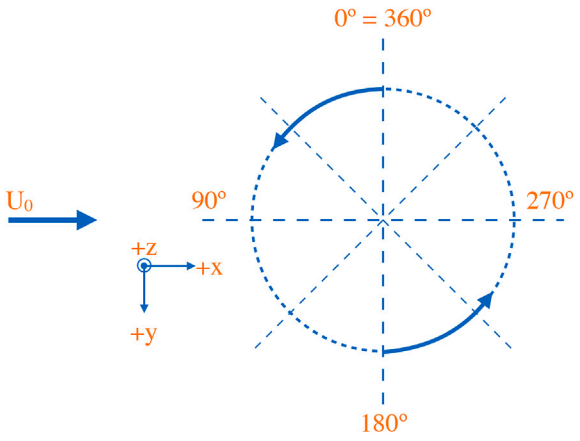

Fig. 4. A schematic representation of the linear and rotational coordinate system.

The wake is represented by the normalised streamwise velocity which is defined by the ratio of the pointwise measured streamwise velocity, u, and the unperturbed wind speed, U_0. The unsteadiness of the flow is defined as the ratio of the streamwise velocity fluctuations σ_u and the average streamwise velocity ($I_u = \frac{\sigma_u}{U_0}$). Because the wake is characterised discretely, a spatial representation of the wakes is presented using contour plots based on linear interpolation.

3. Results

3.1. Isolated vs paired

3.1.1. Streamwise velocity deficit

The wake of an isolated VAWT is compared with the wake of the 1.2D inner-downwind configuration at three heights: $z = 0m$ and $z = \pm 0.25m$ (Fig. 6). The downwind projected boundaries of the rotors are indicated with two solid lines per rotor perpendicular to the abscissa.

The isolated VAWT wake is asymmetric and deflects towards the region behind the upwind moving blade (Fig. 6a to c). This asymmetry is caused by the variation of the aerodynamic forces along θ. Increasing λ reduces this azimuthal variation and will in turn induce a more symmetric wake (Khosravi et al., 2016). The direction of the deflection depends on operating conditions of the VAWT rotors, such as the occurrence of dynamic stall (Boudreau and Dumas, 2017; Peng et al., 2016; Bergeles et al., 1991; Rolin and Porté-Agel, 2015). The two wakes of the 1.2D inner-downwind configuration are similar to the isolated VAWT wake, Fig. 6d to f. A high velocity channel is observed between these two wakes. At mid-span this high velocity channel persists up to $x/D = 6$ and only dissipates after that, Fig. 6e. Some differences with the isolated wake can be observed further downwind around the middle of the paired configuration. Two closely-spaced VAWTs influence each other's incoming flow field by countering the natural deflection of the flow around the middle of the pair (as illustrated by the actuator cylinder (Aagaard Madsen et al., Vita) results in Fig. 7). Paired VAWTs extract more energy near the middle of the pair and in the downwind part of the rotation (Zanforlin and Nishino, 2016; Alexander and Santhanakrishnan, 2020). Because of this, and because of the presence of a second wake (obstructing replenishment), the normalised velocities are lower near the middle of the pair (Fig. 6d to f).

3.1.2. Streamwise flow unsteadiness

Two aerodynamic characteristics are mainly responsible for shed vortices in the wakes of VAWTs and induce unsteadiness in the flow:

1. unsteady aerodynamics around the blades leading to a significant variation of the circulation (also leading to dynamic stall in some cases). Because of the variation of the circulation and Kelvin's theorem (stating that the total circulation moving with the flow is constant), shed vortices are induced along the blade span of a VAWT;
2. Tip vortices at the extremities of the blades which vary in intensity over one rotation due to the varying circulation.

These two characteristics induce distinct unsteady regions and are visualised with horizontal and vertical cross-sections of the wakes (Figs. 8 and 9). Similar to Fig. 6, the black lines on Fig. 8 indicate the downwind projected boundaries of the rotors. Likewise, the frames on Fig. 9 indicate the position of the rotors.

For the isolated configuration, the first region (on Fig. 8b to d, above the upper downwind projected boundary of the rotor and on Fig. 9b at $y/D = -1$ around $z/(H/2) = 0$) arises from the unsteady aerodynamics to which the blades are exposed (Tescione et al., 2014). The reduced frequency, k, allows to estimate the 'magnitude' of the unsteady aerodynamics and can be approximated for VAWTs by the chord-to-diameter ratio (Simão Ferreira, 2009). Because $k > 0.05$ (here $k = 0.1$), the aerodynamics of the rotors induce a significant variation of the

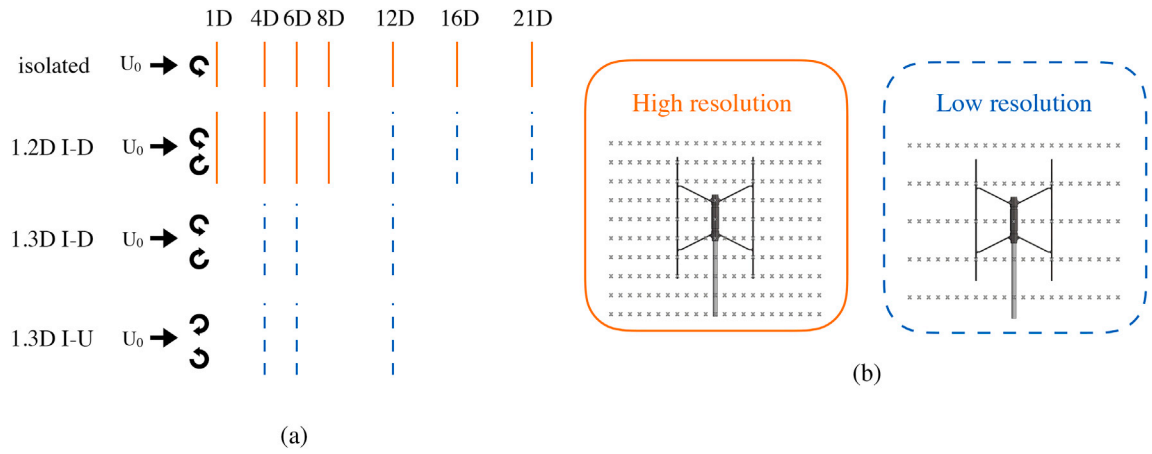

Fig. 5. Schematic top-view (a) and front-view (b) representations of the measurement positions. The solid lines/frame and dashed lines/frame correspond to high- and low-resolution measurements respectively.

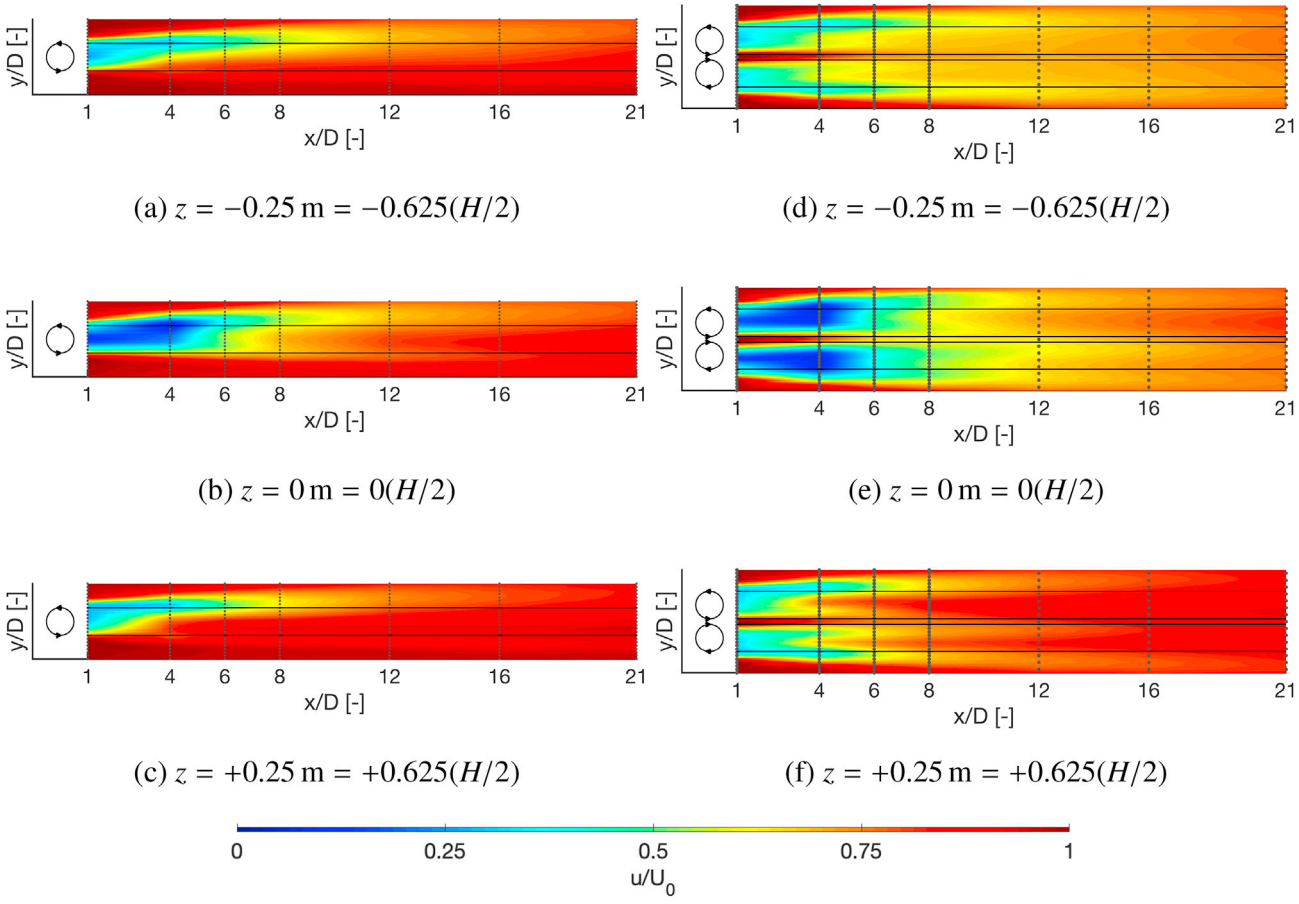

Fig. 6. Streamwise normalised velocities in xy-planes at different heights for the isolated configuration (left) and the 1.2D inner-downwind configuration (right).

circulation around the aerofoil, leading to an unsteady bound vortex. This vortex is at the origin of the free vortices shed in the wake. The most significant variation of the circulation occurs for $0° < \theta < 100°$: the relative velocity to which a VAWT blade is exposed increases as the blade moves upwind and the angle of attack becomes more favourable (De Tavernier et al., 2018). This explains why the highest unsteadiness is behind the upwind moving blade but, similar to the streamwise velocity deficit, the location of this region also depends on the operating conditions of the VAWTs (Battisti et al., Paradiso; Bergeles et al., 1991; Rolin and Porté-Agel, 2015; Posa et al., 2016). The unsteadiness in the flow is also the result of sheared flow as this region corresponds to the edge of the wake, Fig. 6. Furthermore, dynamic stall would induce regions of unsteadiness behind the downwind moving blade. Dynamic stall thus either occurs for $\theta < 90°$ or, more likely, the high λ limits the angles of attack sufficiently as such that dynamic stall does not occur.

Compared to the isolated configuration, the 1.2D inner-downwind configuration also exhibits this zone of increased unsteadiness (Fig. 8g to i outside the downwind projected boundaries and on Fig. 9d at $y/D = \pm 1$ around $z/(H/2) = 0$). The flow unsteadiness is slightly more significant behind the (adjacent) downwind moving blades of the paired configuration than for the isolated configuration. In this region, the high velocity channel between the wakes induces significant shear leading to

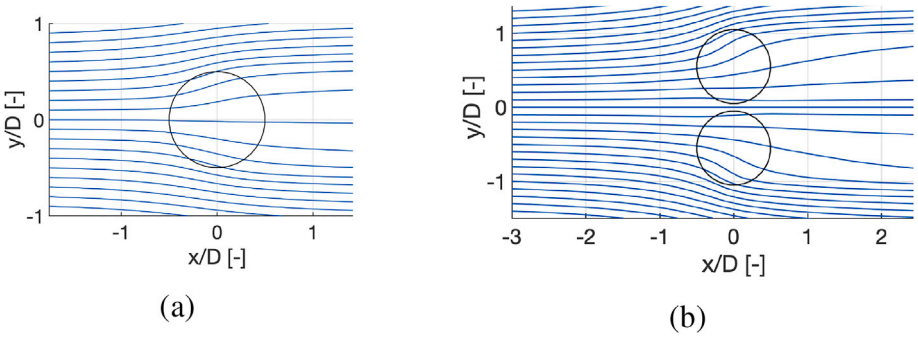

Fig. 7. Flow field based on the actuator cylinder model to illustrate the differences around (a) a single and (b) paired VAWTs (The used actuator cylinder model is described in (De Tavernier and Ferreira, 2019), where it is used for a different application.).

this increased unsteadiness. Some differences may be observed near the middle of the pair (compare the regions behind the downwind moving blades on Fig. 8b to d and Fig. 8g to i, and also the region on Fig. 9b between $0 < y/D < 1$ around $z/(H/2) = 0$ with the region on Fig. 9d, between $-0.60 < y/D < 0.6$ around $z/(H/2) = 0$).

The second region is characterised by the tip vortices. Above and below the turbine (Fig. 8, at planes $z = \pm 0.5m$), tip vortices are the most prominent characteristic in the wake of both configurations (Tescione et al., 2014). These develop in the streamwise direction (on 8a, 8e, 8f and 8j, the unsteady regions follow the downwind projected boundaries or on Fig. 9a and c near $z/(H/2) = \pm 1$). Because $z = \pm 0.5m$ is above or below the rotors, very little momentum is taken from the flow confirming the presence of tip vortices. Noticeably, these tip vortices are not as prominent behind the downwind-moving blade as a result of the locally lower circulation around the aerofoil (De Tavernier et al., 2018).

The wakes of the VAWTs also exhibit central unsteady regions which are caused by the shaft of the turbine. These are most pronounced at $z = 0m$ (Fig. 8c and h), near the top of the shaft. The influence of the shaft is also distinctly noticeable on Fig. 9a near $z/(H/2) = 0$ at $y/D = 0$ or for the paired configuration on Fig. 9c by the two regions at $z/(H/2) = 0$.

3.2. Influence of the direction of rotation

The wakes of the VAWTs deflect towards the region behind the upwind moving blades and in paired configurations the direction of rotation thus influences the wake, Fig. 10. Pairs with inner-downwind moving blades induce and outward deflection: their wake exceeds beyond the downwind projected boundaries of the rotors (black lines on Fig. 10a). This is not the case for the wake of paired VAWTs with inner-upwind moving blades. For this configuration, high-momentum flow is rapidly retrieved beyond the projected boundaries of the pair (the red region beyond the upper and lower black lines of Fig. 10b).

Because of the outward deflected wake for the inner-downwind configuration, interaction between the two individual wakes remains limited. Unsteady flow regions propagate outwards and allow the previously identified vortices to develop freely, Fig. 10c. For the inner-upwind configuration the two individual wakes propagate towards each other inducing substantial interaction and hence unsteadiness behind the middle of the pair, Fig. 10d near $x/D = 4$. This unsteady region dissipates rapidly and is suggestive of vortex suppression (Chan et al., 2011; Craig et al., Koseff).

Fig. 11 shows contour plots of the streamwise velocity deficits in several yz-planes. The lateral velocity components are plotted above by means of vectors and are discussed in Section 3.3. On Fig. 11a, the two wakes of the inner-downwind pair remain distinguishable. Each wake clearly extends higher and lower behind the upwind moving blades, induced by the more important tip vortices on that side ($y/D = \pm 1$). On the downwind moving part of the rotation, tip vortices are so small that they barely induce a streamwise velocity deficit. Further downwind ($x/D = 12$, Fig. 11c), the outwards expansion results in a relatively large region of reduced normalised velocities. At $x/D = 12$, the velocity in the wake is approximately $0.75U_0$, which covers a region larger than the dimensions of the rotors. On the other hand, the inner-upwind configuration exhibits a unified wake (Fig. 11d). Further downstream (Fig. 11f), the wake is centrally contained in a region where $u = 0.5U_0$. This region migrates downwards behind the centre of the pair, where the floating floor obstructs replenishment from the bottom. Outside of this low-velocity flow, the normalised velocities range around 90 of the unperturbed flow for the regions beyond $y/D = \pm 1$.

3.3. Replenishment mechanisms

On Fig. 11, the sums of the *v*- and *w*-velocity components are indicated with vectors and illustrate the different wake replenishment mechanisms. A normalised vector with magnitude 1 is added as a reference (vector with symbol $\overrightarrow{1_y}$). The vectors on Fig. 11a indicate an important replenishment of the wake of the 1.3D inner-downwind configuration from the top centre region of the wake. As observed by Rolin and Porté-Agel (2018), the upper replenishment is influenced by the tip vortices (around $z/(H/2) = 1$). The replenishment from the bottom is less substantial because of the presence of the floor.

For the inner-upwind configuration, *v* and *w* indicate that the wake replenishment occurs mostly downwind of the upper, outer corners (Fig. 11d). The flow in the wake contains a downward vertical component which explains the bottom-concentrated wake at $x/D = 12$ (Fig. 11f). Furthermore, vortex-like motions can be identified. For the 1.3D inner-downwind configuration, four rotating motions are identifiable at $x/D = 6$. These are less easily distinguishable for the 1.3D inner-upwind configuration (Fig. 11e). Here, the horizontal contraction of the wake induces a central spanwise expansion of the wake.

The general perpendicular velocity components in the wake for both configurations are presented schematically in Fig. 12. The schematic is based on the wake at $x = 6D$, i.e. Fig. 11b and e (it can be noted that the flow structures are slightly different at $x = 4D$). Several studies have identified similar vortex-like motions in studies of the wakes of isolated (Rolin and Porté-Agel, 2018; Ryan et al., 2016) or paired VAWTs (Lam and Peng, 2016; Brownstein et al., 2019).

4. Quantitative wake properties

We define the following nomenclature to ease the quantitative comparison of the properties of the wake (Fig. 13):

- The equivalent diameter $D_{eq} = 2D + s$, with *s* the spacing between the VAWT rotors. This equivalent diameter is used to normalise distances for the paired configurations;
- The lowest normalised velocity retrieved per considered velocity profile is indicated with $(u/U_0)_{min}$;

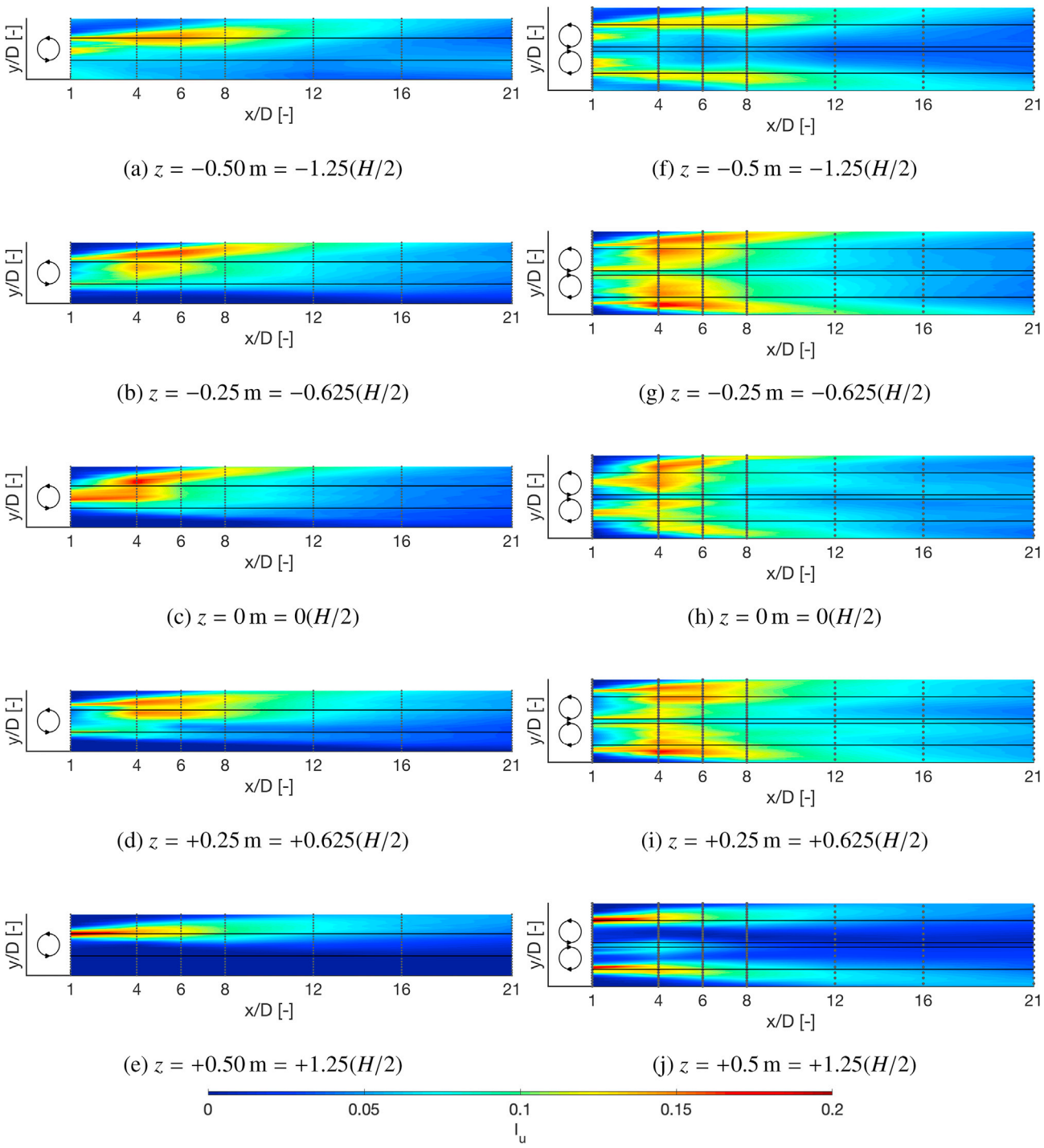

Fig. 8. Flow unsteadiness in xy-planes at different heights for the isolated configuration (left) and the 1.2D inner-downwind configuration (right).

- The lateral distance ψ (normalised by D_{eq}) between $(u/U_0)_{min}$ and the lateral centre of the configuration. Note that the position of $y/D = 0$ differs for the isolated and paired configurations.
- The wake width δ (normalised by D_{eq}) between the points where the velocity reaches 80% of U_0. For paired configurations it includes the region between the turbines, regardless whether the speed is above or below $0.8U_0$. The choice for 80% (as opposed to the customary 99%) was required to guarantee that end points were found within the spatial range for all downstream positions;
- The highest retrieved magnitude of unsteadiness per considered velocity profile $I_{u,max}$.

Note that, for the quantitative comparison of the wakes in different configurations, the analysis is reduced to a two-dimensional analysis at the mid-plane $z = 0m$.

4.1. General development of the velocity profiles

Fig. 14 illustrates the velocity profiles at different downwind distances of a VAWT rotor in isolation and in paired configurations. The velocity profiles of the isolated rotor are plotted in order to allow comparison with a rotor in paired configuration turning the same direction. Several observations can be made:

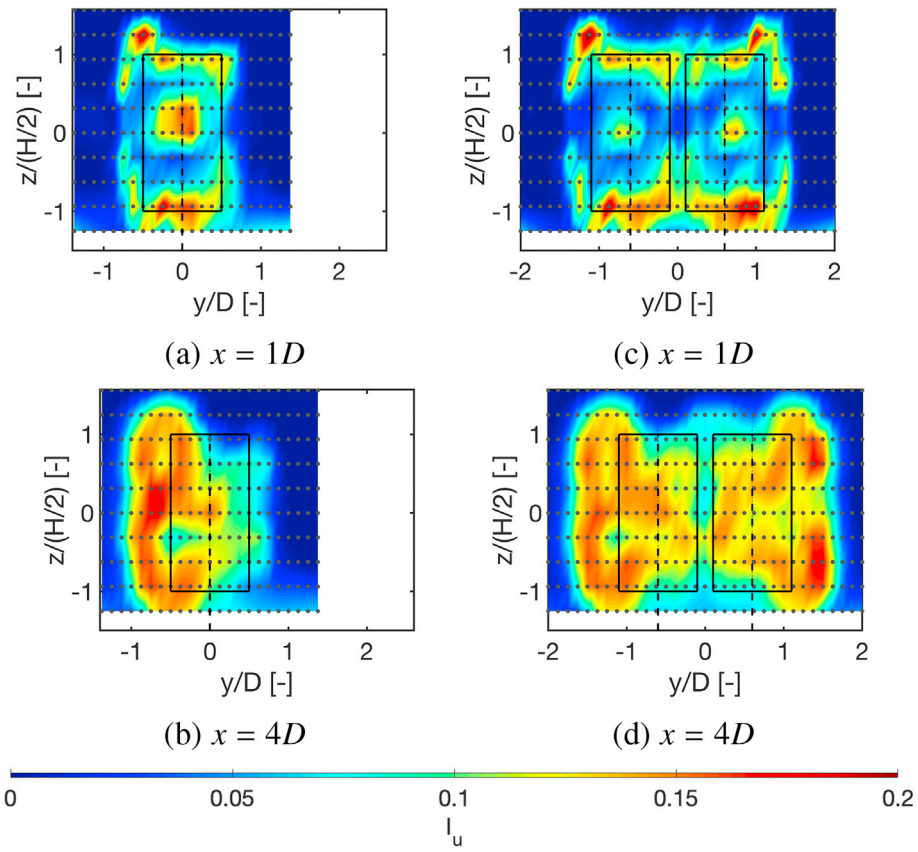

Fig. 9. Flow unsteadiness at two downwind positions behind the isolated configuration (left) and 1.2D inner-downwind configuration (right).

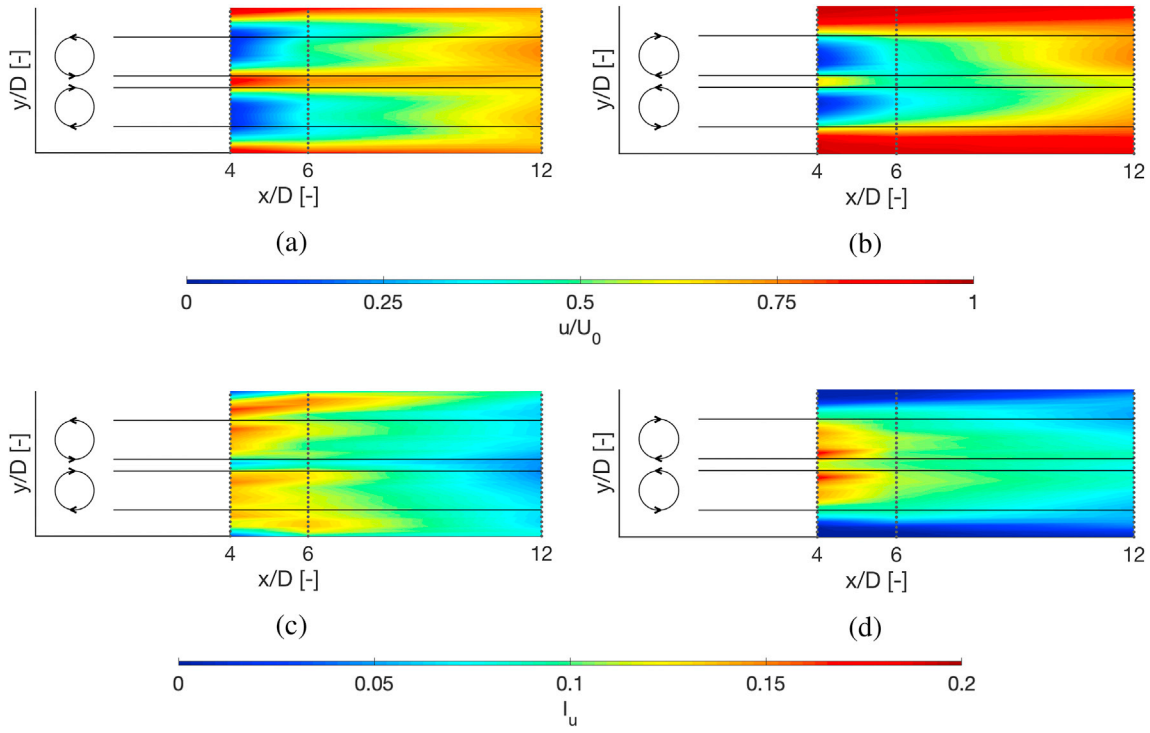

Fig. 10. Streamwise normalised velocities and streamwise flow unsteadiness in xy-planes at $z = 0m = H/2$ for the 1.3D inner-downwind configuration (left) and the 1.3D inner-upwind configuration (right).

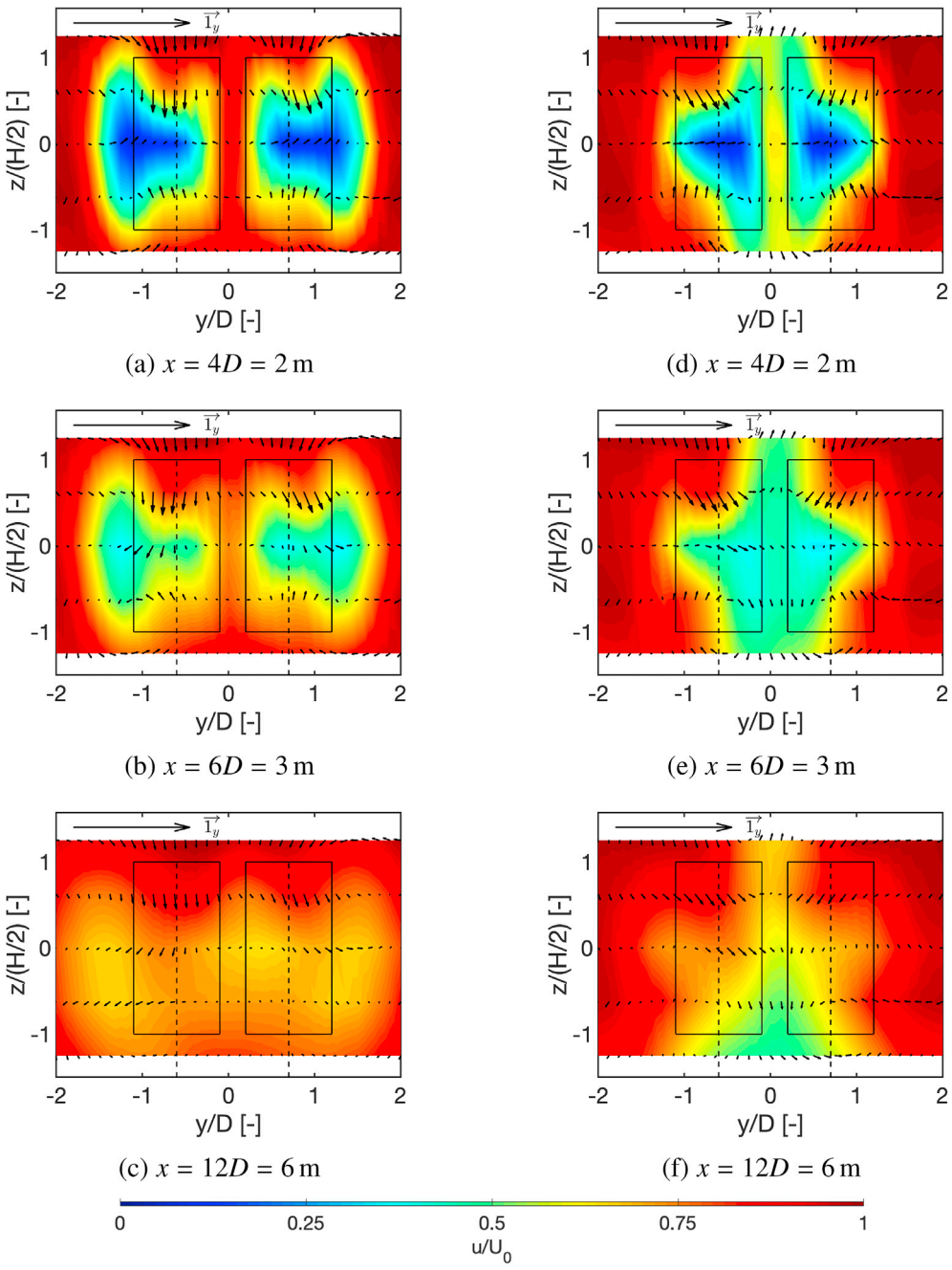

Fig. 11. The image of the wake of paired VAWTs depends on the direction of the inner moving blades. Left: 1.3D inner-downwind moving blades, right: 1.3D inner-upwind moving blades. On top of each contour plot, an arrow is added to illustrate magnitude 1.

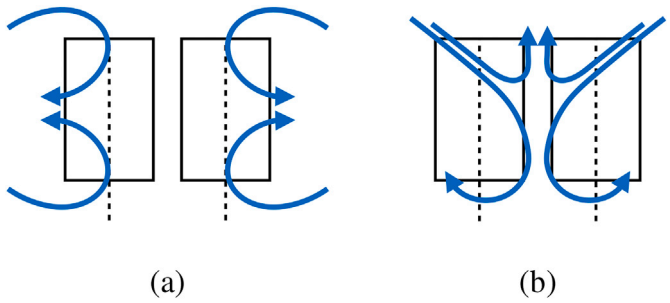

Fig. 12. Schematic representation of the general replenishment of the wake of the inner-downwind configuration (a) and inner-upwind configuration (b).

- At $x/D = 1$, the normalised velocity for the 1.2D inner-downwind configuration is higher at $y/D = 0$ than for the isolated configuration (Fig. 14a).
- The initial high velocity channel between the turbine starts to dissipate from $x/D > 4$ because of turbulent mixing, Fig. 14a. From $x/D = 8$ onwards, the wake has a relatively uniform shape and at $x/D = 21$, a deficit of 20 is still present.
- The velocity profiles in the wake of inner-downwind configurations are similar to the isolated configuration (blue and orange curve overlap on Fig. 14a and b).
- For the inner-upwind configuration, the deflection of the wakes is obstructed because of the adjacent wake and induces different shapes of the velocity profiles (blue and orange curve do not overlap on Fig. 14c).

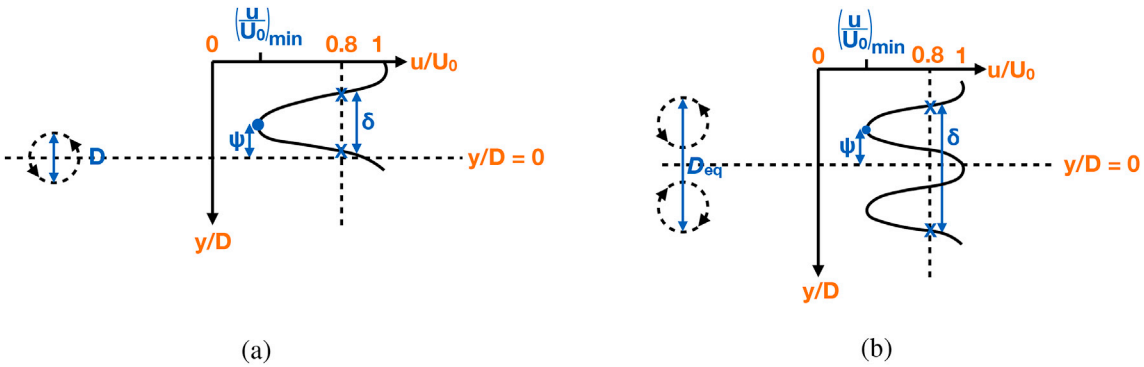

Fig. 13. Schematic of a velocity profile to indicate the nomenclature of the isolated (a) and paired (b) wake properties.

- The inner-upwind configuration exhibits a small recovery delay in the far wake, e.g. at $x/D = 12$ (Fig. 14c).
- Regions where the rate of change of u/U_0 is large with respect to y/D induce significant shear and hence turbulence. The flow in the centre of the inner-downwind wake will be more subjected to shear than in the centre of the wake of inner-upwind configurations (compare velocity profiles at $x/D = 6$ near $y/D = 0$).

4.2. Velocity deficit

The decay of $(u/U_0)_{min}$ is similar for the isolated and paired configurations (Fig. 15a). Around $x/D = 4$, $(u/U_0)_{\min} \approx 0.07$ for all configurations. At $x/D = 12$, the isolated configuration has recovered to about $0.75U_0$. This is only 3 higher than for the two inner-downwind configurations. The inner-upwind configuration exhibits a recovery of $(u/U_0)_{\min}$ to just over 60. Considering D and D_{eq}, the 75% recovery occurs at $x/D_{eq} = 5.4$ for the 1.2D inner-downwind configuration and $x/D_{eq} = 5.2$ for the 1.3D inner-downwind configuration.

4.3. Lateral migration

For $x/D = 4$, ψ is identical for the isolated configuration and the inner-downwind configurations, Fig. 15b. From $x/D > 4$, ψ increases more significantly for the isolated configuration than for inner-downwind pairs. For the inner-upwind configuration, ψ continuously decreases and at $x/D_{eq}(1.3D) = 5.2$, $\psi \approx 0$ indicates that $(u/U_0)_{min}$ is located at the middle of the pair. (The large difference of ψ between the isolated and 1.2D inner-downwind configuration at $x/D = 1$ is explained by the different positions of $y/D = 0$.)

4.4. Width

At $x/D = 8$, the wakes of the inner-downwind pairs expand up to $1.6D_{eq}$ while the isolated configuration exhibits an expansion of $1.8D$ at $x/D = 8$ (Fig. 15c). Further downstream the $0.8U_0$ limit is almost reached explaining the abrupt narrowing of the isolated wake. The 1.3D inner-upwind wake barely expands but rather contracts as it develops.

4.5. Flow unsteadiness

Both inner-downwind configurations exhibit levels of I_u similar to the isolated configuration as these unsteady regions are mostly at the outside edges of the wake. For the 1.3D inner-upwind configuration the unsteady region is near the middle of the pair, where the flow also benefits from an acceleration. The unsteadiness in the flow dissipates rapidly for this configuration (Fig. 15d).

4.6. Comparison with literature

Previously, Lam and Peng (2016) reported on wake measurements of co- and counter-rotating VAWTs. Table 1 compares design and operational parameters of their study with the present study. The most notable differences are the tip-speed ratio, rotor solidity σ and inter-turbine distance. To identify the influence of operational parameters or geometrical parameters, both studies are compared based on mid-span velocity profiles at 4D and 6D, Fig. 16.

At 4D, the velocity deficit observed in this study is significantly larger than the one observed by Lam and Peng. These differences are likely to be caused by different power coefficients (no power coefficient is reported in (Lam and Peng, 2016)). Furthermore, the velocity deficit measured by Lam and Peng appears to be sensitive to the direction of rotation, i.e. velocities are higher for the inner-upwind configuration than for the inner-downwind configuration (Figs. 16a and b vs Fig. 16c and d). This effect is not observed in the present study and the influence is likely to be caused by the different values of λ. At $\lambda = 1$, dynamic stall will be prominently present. The authors hypothesize here that the azimuthal angle at which dynamic stall occurs is sensitive to the proximity of a second VAWT. This sensitivity depends whether dynamic stall occurs around the middle of the pair or at the outer edges of the pair. For the inner-downwind configuration, dynamic stall vortices will be shed at the outer edges of the pair. However, for the inner-upwind configuration, dynamics stall vortices are shed near the middle of the pair, in the central high velocity channel. Such differences are believed to induce different velocities in the wake according to the direction of rotation.

The inter-turbine spacing in the study of Lam and Peng is 2D. In the inner-upwind configuration (Fig. 16c and d) the minimal velocity is retrieved at the same absolute y/D-values for both studies. A more pronounced deflection of the wake is thus observed in the study of Lam and Peng. Different values of λ are again expected to be the cause for the different deflections. The mechanical power of a turbine is defined by $P_{mech} = \tau\omega$ (τ = torque, ω = rotational speed). For a slow turning VAWT, the ratio τ/ω is larger than for a fast turning VAWT (considering similar power coefficients). This suggests that the deflection of the wake is most influenced by the reaction to the aerodynamic forces, which engage on the flow.

Lastly, Lam and Peng conclude that the average velocity in the wake of the inner-upwind configuration recovers to approximately 80 at a downwind distance of $2D_{eq}$. In this study, an 80 recovery of the average velocity in the wake is only observed at $5.2D_{eq}$.

5. Conclusions

This experimental study demonstrates the influence of pairing VAWTs on their wakes. Different directions of rotation of paired VAWTs induce very different wakes. Paired configurations where the middle blades move downwind induce a similar wake as isolated configurations. This is

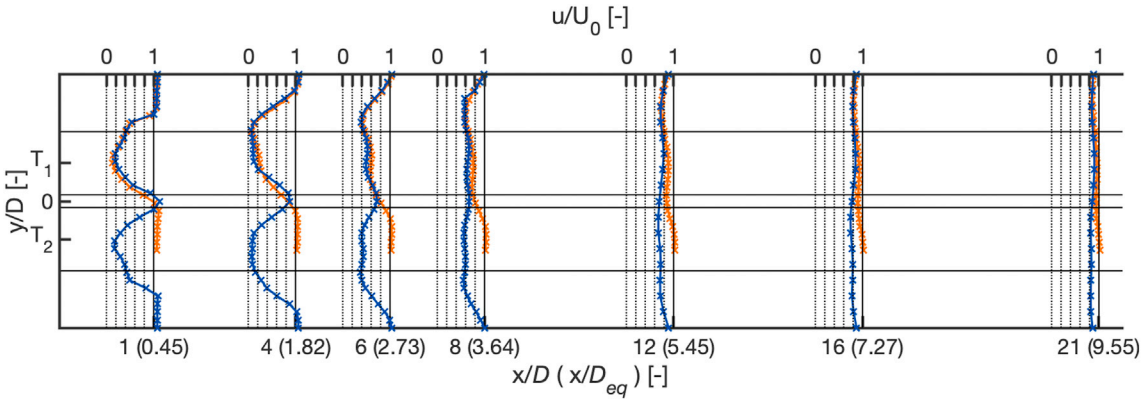

(a) Isolated configuration vs 1.2D inner-downwind configuration

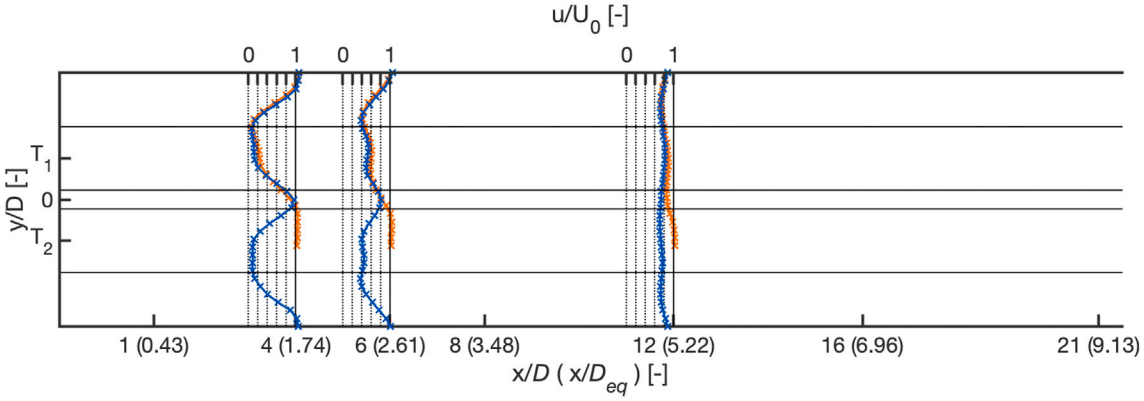

(b) Isolated configuration vs 1.3D inner-downwind configuration

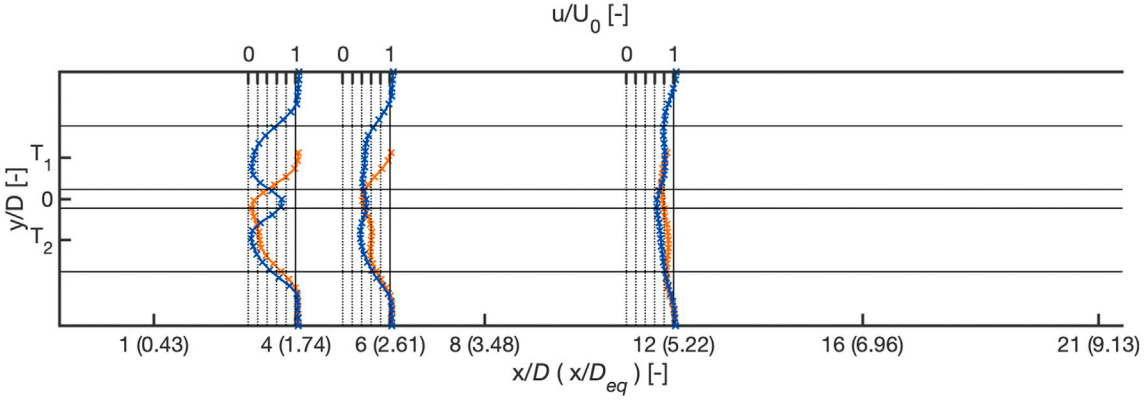

(c) Isolated configuration vs 1.3D inner-upwind configuration

Fig. 14. The numerical values of the velocity profiles at $z = 0$ for several downwind positions where the isolated configuration (orange) is compared to the paired configurations (blue). (For interpretation of the references to colour in this figure legend, the reader is referred to the Web version of this article.)

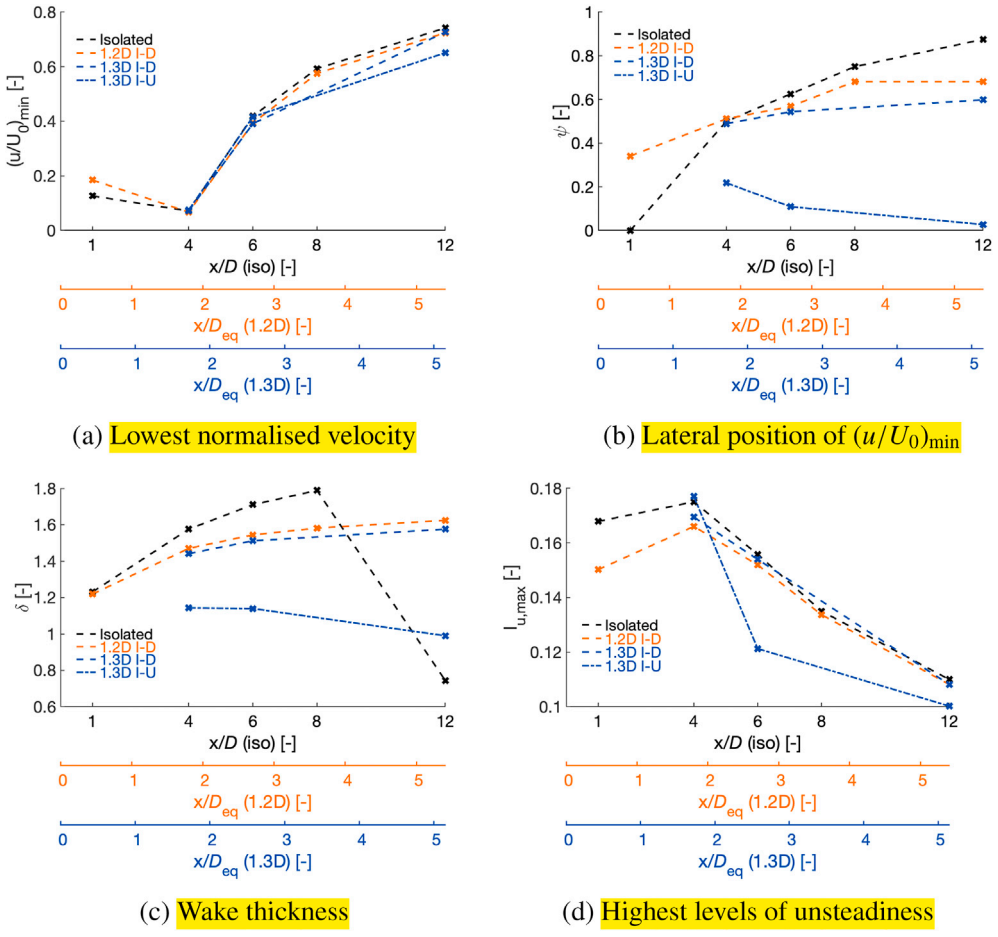

Fig. 15. Comparison of the wake properties for the isolated configuration and the paired configurations. The three abscissa scales correspond to downwind distances normalised with D or D_{eq}.

Table 1
Comparison of the design and operation parameters between the rotors of Lam and Peng (2016) and the present study.

	Lam and Peng	Present
Rotor type	H-Darrieus	H-Darrieus
Number of blades	5	2
Diameter, D [m]	0.300	0.500
Height, H [m]	0.300	0.800
Blade chord, c [m]	0.060	0.050
Solidity, σ [-]	1.0	0.2
Tip-speed ratio, λ [-]	1.0	3.0
Unperturbed velocity, U_0 [m/s]	12.8	10.7
Turbulence intensity, I_0 [-]	1.11	2.0
Blockage ratio, ε [-]	3.6	2
Reynolds number, Re_c [-]	1.7×10^5	1.0×10^5
Inter-turbine distance [-]	2D	1.2–1.3D

because the deflection of the wake is directed outwards. For inner-upwind pairs, the wake is unified and centred. In such a configuration, the wakes deflect towards each other inducing a centrally narrow wake.

The lengths of the wakes of the studied paired configurations are similar to the isolated configuration but the wake of the inner-upwind configuration exhibits a small delay of the recovery. The wake width of inner-downwind configurations is also comparable to the isolated configuration while the inner-upwind configuration induces a much smaller wake. Finally, the replenishment mechanisms also differ significantly based on the direction of rotation. Similar to previous observations on isolated VAWT wakes, tip vortices appear to play an important role for the replenishment of the wake of inner-downwind configurations. This replenishment mechanism seems to be influenced for inner-upwind configurations. Here, the horizontal contraction of the wake induces a central spanwise expansion of the wake.

Pairing VAWTs exhibits advantages with regards to the performance (e.g. (Vergaerde et al., 2020)) and can potentially be used for applications in wind farms. For floating offshore applications, the benefits of paired VAWTs can be complemented with benefits for the floating platforms. Two side by side VAWTs placed on a same platform have several advantages: an increased performance, a narrow wake (considering the wake of paired VAWTs vs two wakes of isolated VAWTs), the possibility to induce a zero net-generator torque on a floating platform and the possibility to orient the platform by varying the torque of each rotor individually.

CRediT authorship contribution statement

Antoine Vergaerde: Methodology, Formal analysis, Investigation, Writing - original draft, Visualization. **Tim De Troyer:** Conceptualization, Methodology, Validation, Writing - original draft, Supervision. **Sara Muggiasca:** Methodology, Formal analysis, Investigation, Writing - original draft, Visualization. **Ilmas Bayati:** Conceptualization, Methodology, Validation, Writing - review & editing, Resources. **Marco Belloli:** Conceptualization, Writing - review & editing, Resources, Project administration, Funding acquisition. **Joanna Kluczewska-Bordier:** Conceptualization, Resources, Writing - review & editing, Supervision. **Nicolas Parneix:** Formal analysis, Investigation, Methodology, Validation, Writing - review & editing. **Frederic Silvert:** Conceptualization,

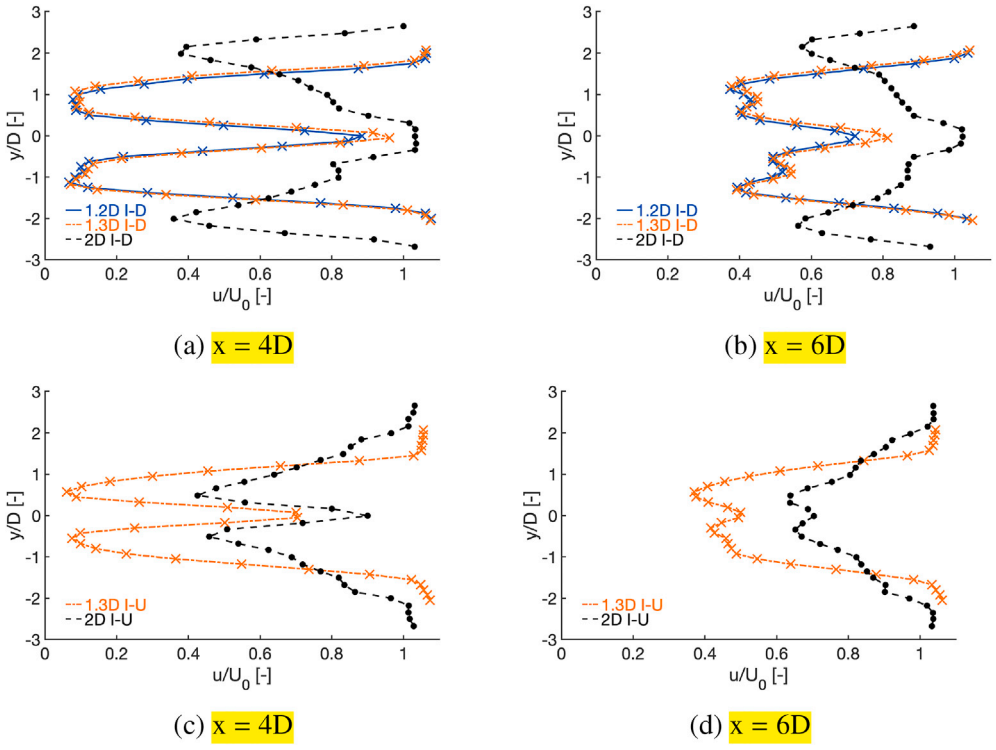

Fig. 16. Comparison of the velocity profiles in the wake at $z = 0m$ of the present study with the data of Lam and Peng (Lam and Peng, 2016) in black.

Writing - review & editing, Project administration, Funding acquisition. **Mark C. Runacres:** Conceptualization, Software, Data curation, Writing - review & editing, Project administration, Funding acquisition.

Declaration of competing interest

The authors declare that they have no known competing financial interests or personal relationships that could have appeared to influence the work reported in this paper.

Acknowledgements

The authors would like to thank Alain Wery and Lieven Standaert from the Vrije Universiteit Brussel and Luca Ronchi from the Politecnico di Milano for their technical support. The authors would also like to thank Denis Pitance and professor S. Zanforlin for their valuable help and suggestions. The financial support of Nenuphar and of the department of Engineering Technology is acknowledged.

References

H. Aagaard Madsen, T. J. Larsen, U. Schmidt Paulsen, L. Vita, Implementation of the actuator cylinder flow model in the HAWC2 code for aeroelastic simulations on vertical Axis wind turbines, Proceedings of 51st AIAA Aerospace Sciences Meeting Including the New Horizons Forum and Aerospace Exposition .

Abkar, M., Dabiri, J.O., 2017. Self-similarity and flow characteristics of vertical-axis wind turbine wakes: an LES study. J. Turbul. 18 (4), 373–389.

Alexander, A.S., Santhanakrishnan, A., 2020. Mechanisms of power augmentation in two side-by-side vertical axis wind turbines. Renew. Energy 148, 600–610.

Araya, D.B., Dabiri, J.O., 2015. A comparison of wake measurements in motor-driven and flow-driven turbine experiments. Exp. Fluid 56 (7), 150.

Bachant, P., Wosnik, M., 2015. Characterising the near-wake of a cross-flow turbine. J. Turbul. 16 (4), 392–410.

Bachant, P., Wosnik, M., 2016. Effects of Reynolds number on the energy conversion and near-wake dynamics of a high solidity vertical-Axis cross-flow turbine. Energies 9 (2), 73.

L. Battisti, L. Zanne, S. Dell'Anna, V. Dossena, G. Persico, B. Paradiso, Aerodynamic measurements on a vertical Axis wind turbine in a large scale wind tunnel, J. Energy Resour. Technol. 133 (3).

Bergeles, G., Michos, A., Athanassiadis, N., 1991. Velocity vector and turbulence in the symmetry plane of a Darrieus wind generator. J. Wind Eng. Ind. Aerod. 37 (1), 87–101.

Bilgili, M., Yasar, A., Simsek, E., 2011. Offshore wind power development in Europe and its comparison with onshore counterpart. Renew. Sustain. Energy Rev. 15 (2), 905–915.

Borg, M., Collu, M., 2015. A comparison between the dynamics of horizontal and vertical axis offshore floating wind turbines. Phil. Trans. Math. Phys. Eng. Sci. 373, 20140076, 2035.

Borg, M., Shires, A., Collu, M., 2014. Offshore floating vertical axis wind turbines, dynamics modelling state of the art. part I: Aerodynamics. Renew. Sustain. Energy Rev. 39 (Suppl. C), 1214–1225.

Boudreau, M., Dumas, G., 2017. Comparison of the wake recovery of the axial-flow and cross-flow turbine concepts. J. Wind Eng. Ind. Aerod. 165, 137–152.

Brownstein, I.D., Wei, N.J., Dabiri, J.O., 2019. Aerodynamically interacting vertical-Axis wind turbines: performance enhancement and three-dimensional flow. Energies 12 (14), 2724.

Bull, D.L., Fowler, M., Goupee, A., 2014. A Comparison of Platform Options for Deep-Water Floating Offshore Vertical Axis Wind Turbines: an Initial Study., Tech. Rep. SAND2014-16800. Sandia National Lab. (SNL-NM), Albuquerque, NM (United States).

Campagnolo, F., Petrović, V., Schreiber, J., Nanos, E.M., Croce, A., Bottasso, C.L., 2016. Wind tunnel testing of a closed-loop wake deflection controller for wind farm power maximization. J. Phys. Conf. 753, 032006.

Chan, A.S., Dewey, P.A., Jameson, A., Liang, C., Smits, A.J., 2011. Vortex suppression and drag reduction in the wake of counter-rotating cylinders. J. Fluid Mech. 679, 343–382.

A. E. Craig, J. O. Dabiri, J. R. Koseff, A kinematic description of the key flow characteristics in an array of finite-height rotating cylinders, J. Fluid Eng. 138 (7).

Dabiri, J.O., 2011. Potential order-of-magnitude enhancement of wind farm power density via counter-rotating vertical-axis wind turbine arrays. J. Renew. Sustain. Energy 3 (4), 043104.

De Tavernier, D., Ferreira, C., 2019. An extended actuator cylinder model: actuator-in-actuator cylinder (AC-squared) model. Wind Energy 22 (8), 1058–1070.

De Tavernier, D., Ferreira, C., Li, A., Paulsen, U., Madsen, H., 2018. Towards the understanding of vertical-axis wind turbines in double-rotor configuration. J. Phys. Conf. 1037, 022015.

Dossena, V., Persico, G., Paradiso, B., Battisti, L., Dell'Anna, S., Brighenti, A., Benini, E., 2015. An experimental study of the aerodynamics and performance of a vertical Axis wind turbine in a confined and unconfined environment. J. Energy Resour. Technol. 137 (5), 051207.

Duraisamy, K., Lakshminarayan, V., 2014. Flow physics and performance of vertical Axis wind turbine arrays. In: 32nd AIAA Applied Aerodynamics Conference, vol. 3139. American Institute of Aeronautics and Astronautics.

Fleming, P., Annoni, J., Shah, J.J., Wang, L., Ananthan, S., Zhang, Z., Hutchings, K., Wang, P., Chen, W., Chen, L., 2017. Field test of wake steering at an offshore wind farm. Wind Energy Science 2 (1), 229–239.
Gebraad, P.M.O., Teeuwisse, F.W., van Wingerden, J.W., Fleming, P.A., Ruben, S.D., Marden, J.R., Pao, L.Y., 2016. Wind plant power optimization through yaw control using a parametric model for wake effects—a CFD simulation study. Wind Energy 19 (1), 95–114.
Hand, B., Cashman, A., 2020. A review on the historical development of the lift-type vertical axis wind turbine: from onshore to offshore floating application. Sustain.Energy.Technol. Assessments 38, 100646.
Hohman, T.C., Martinelli, L., Smits, A.J., 2018. The effects of inflow conditions on vertical axis wind turbine wake structure and performance. J. Wind Eng. Ind. Aerod. 183, 1–18.
Howell, R., Qin, N., Edwards, J., Durrani, N., 2010. Wind tunnel and numerical study of a small vertical axis wind turbine. Renew. Energy 35 (2), 412–422.
Kadum, H., Friedman, S., Camp, E.H., Cal, R.B., 2018. Development and scaling of a vertical axis wind turbine wake. J. Wind Eng. Ind. Aerod. 174, 303–311.
Kadum, H., Cal, R.B., Quigley, M., Cortina, G., Calaf, M., 2020. Compounded energy gains in collocated wind plants: energy balance quantification and wake morphology description. Renew. Energy 150, 868–877.
Kanner, S.A.C., 2015. Design, Analysis, Hybrid Testing and Orientation Control of a Floating Platform with Counter-rotating Vertical-Axis Wind Turbines. Ph.D. thesis. UC Berkeley.
S. Kanner, E. Koukina, R. W. Yeung, Power optimization of model-scale floating wind turbines using real-time hybrid testing with autonomous actuation and control, J. Offshore Mech. Arctic Eng. 141 (3).
Khosravi, M., Sarkar, P., Hu, H., 2016. An experimental investigation on the near wake characteristics of a darrious vertical-Axis wind turbine. In: 34th Wind Energy Symposium, vols. 1–11. American Institute of Aeronautics and Astronautics.
Kinzel, M., Mulligan, Q., Dabiri, J.O., 2012. Energy exchange in an array of vertical-axis wind turbines. J. Turbul. 13, N38.
Lam, H.F., Peng, H.Y., 2016. Study of wake characteristics of a vertical axis wind turbine by two- and three-dimensional computational fluid dynamics simulations. Renew. Energy 90 (Suppl. C), 386–398.
Lei, H., Su, J., Bao, Y., Chen, Y., Han, Z., Zhou, D., 2019. Investigation of wake characteristics for the offshore floating vertical axis wind turbines in pitch and surge motions of platforms. Energy 166, 471–489.
Parneix, N., Fuchs, R., Immas, A., Silvert, F., Deglaire, P., 2016. Efficieny improvement of vertical-axis wind turbines with counter-rotating lay-out. Proceedings of the EWAE 1–8.
Paulsen, U.S., Madsen, H.A., Hattel, J.H., Baran, I., Nielsen, P.H., 2013. Design optimization of a 5 MW floating offshore vertical-axis wind turbine. Energy Procedia 35 (Suppl. C), 22–32.
Peng, H.Y., Lam, H.F., Lee, C.F., 2016. Investigation into the wake aerodynamics of a five-straight-bladed vertical axis wind turbine by wind tunnel tests. J. Wind Eng. Ind. Aerod. 155, 23–35.
Posa, A., 2019. Wake characterization of coupled configurations of vertical axis wind turbines using Large Eddy Simulation. Int. J. Heat Fluid Flow 75, 27–43.
Posa, A., Parker, C.M., Leftwich, M.C., Balaras, E., 2016. Wake structure of a single vertical axis wind turbine. Int. J. Heat Fluid Flow 61, 75–84.
Rezaeiha, A., Montazeri, H., Blocken, B., 2018a. Characterization of aerodynamic performance of vertical axis wind turbines: impact of operational parameters. Energy Convers. Manag. 169, 45–77.
Rezaeiha, A., Montazeri, H., Blocken, B., 2018b. Towards optimal aerodynamic design of vertical axis wind turbines: impact of solidity and number of blades. Energy 165, 1129–1148.
Rolin, V., Porté-Agel, F., 2015. Wind-tunnel study of the wake behind a vertical axis wind turbine in a boundary layer flow using stereoscopic particle image velocimetry. J. Phys. Conf. 625, 012012.
Rolin, V.F.-C., Porté-Agel, F., 2018. Experimental investigation of vertical-axis wind-turbine wakes in boundary layer flow. Renew. Energy 118, 1–13.
Ross, I., Altman, A., 2011. Wind tunnel blockage corrections: review and application to Savonius vertical-axis wind turbines. J. Wind Eng. Ind. Aerod. 99 (5), 523–538.
Ryan, K.J., Coletti, F., Elkins, C.J., Dabiri, J.O., Eaton, J.K., 2016. Three-dimensional flow field around and downstream of a subscale model rotating vertical axis wind turbine. Exp. Fluid 57 (3), 38.
Simão Ferreira, C.J., 2009. The Near Wake of the VAWT: 2D and 3D Views of the VAWT Aerodynamics. Ph.D. thesis. TU Delft.
Taboada, J.V., 2016. Comparative analysis review on floating offshore wind foundations (FOWF). Naval .Eng.Maritime.Ind.Congr 54th (949), 75–87.
Tescione, G., Ragni, D., He, C., Simão Ferreira, C.J., van Bussel, G.J.W., 2014. Near wake flow analysis of a vertical axis wind turbine by stereoscopic particle image velocimetry. Renew. Energy 70, 47–61.
Tjiu, W., Marnoto, T., Mat, S., Ruslan, M.H., Sopian, K., 2015. Darrieus vertical axis wind turbine for power generation II: challenges in HAWT and the opportunity of multi-megawatt Darrieus VAWT development. Renew. Energy 75, 560–571.
Vergaerde, A., De Troyer, T., Carbó Molina, A., Standaert, L., Runacres, M.C., 2019. Design, manufacturing and validation of a vertical-axis wind turbine setup for wind tunnel tests. J. Wind Eng. Ind. Aerod. 193, 103949.
Vergaerde, A., De Troyer, T., Standaert, L., Kluczewska-Bordier, J., Pitance, D., Immas, A., Silvert, F., Runacres, M.C., 2020. Experimental validation of the power enhancement of a pair of vertical-axis wind turbines. Renew. Energy 146, 181–187.
Xie, S., Archer, C.L., Ghaisas, N., Meneveau, C., 2017. Benefits of collocating vertical-axis and horizontal-axis wind turbines in large wind farms. Wind Energy 20 (1), 45–62.
Zanforlin, S., Nishino, T., 2016. Fluid dynamic mechanisms of enhanced power generation by closely spaced vertical axis wind turbines. Renew. Energy 99 (Suppl. C), 1213–1226.